THE UNIVERSITY of EDINBURGH

Edinburgh Research Explorer

Numerical analysis of solar chimney power plant integrated with CH4 photocatalytic reactors for fighting global warming under ambient crosswind

OPEN ACCESS

Numerical analysis of solar chimney power plant integrated with CH$_4$ photocatalytic reactors for fighting global warming under ambient crosswind

Abstract: Methane's global warming potential (GWP) is much larger than carbon dioxide and contributes significantly to global warming. Solar chimney power plant (SCPP) integrated with photocatalytic reactors can capture and remove atmospheric methane, and generate electrical power without fossil energy consumption simultaneously. In this paper, the performance of the flow characteristics, the CH$_4$ removal, the CO$_2$ emission reduction, and the power generation were analyzed for the SCPP integrated with different types of photocatalytic reactors under ambient crosswind (ACW). The results revealed that the SCPP integrated with a honeycomb reactor was more stable for the degradation of CH$_4$ than that with a plate reactor. With an increase in ACW, the removal rate of atmospheric CH$_4$ was reduced to a constant value of 0.41g/s for the honeycomb reactor and 0.11g/s for the plate reactor. The SCPP integrated with a honeycomb reactor achieved a maximum power generation of 88.31 kW, which was 1.63 times than that of the conventional SCPP when $G = 857$ W/m^2 and ACW = 0 m/s. In addition, the improved SCPP could reduce CO$_2$ emissions by 85.04 kg/h when $G = 857$ W/m^2, ACW = 0 m/s, and $\triangle P = 320$ Pa.

Nomenclature	
B, B_1, B_2	Constants for reaction rate of CH$_4$
$C_{1\varepsilon}, C_{2\varepsilon}$	Constants for turbulent model
c_1	CH$_4$ concentration at inlet of the canopy, $mol \cdot m^{-3}$
c_2	O$_2$ concentration at outlet of the chimney, $mol \cdot m^{-3}$
m_1	CH$_4$ mass fraction at the entrance of reactors
m_2	CH$_4$ mass fraction at the exit of reactors

r_m	Reaction rate of CH$_4$ in honeycomb reactor, $mol \cdot W^{-1} \cdot m^{-1} \cdot s^{-1}$
r_{AI}	Reaction rate of CH$_4$ in plate reactor, $mol \cdot W^{-1} \cdot s^{-1}$
G	Solar radiation, $W \cdot m^{-2}$
q	Heat flux, $W \cdot m^{-2}$
SSA	Specific surface area, m^{-1}
$\vec{J_i}$	Diffusion flux of species i, $mol \cdot s^{-1} \cdot m^{-3}$
Q_m	Mass flow rate, $kg \cdot s^{-1}$
$\dot{m}_{CH_4}$	Purification rate of CH$_4$, $g \cdot s^{-1}$
W_e	Output power of system, kW
Δp	Pressure drop of the turbine, Pa
S_Φ	Momentum loss, $N \cdot m^{-3}$
S_i	Additional rate, $kg \cdot m^{-3} \cdot s^{-1}$
C_{eq}	CO$_2$ equivalent
$\dot{C}_{eq}$	Rate of CO$_2$ reduction, $kg \cdot h^{-1}$

Greek symbols

v	Kinetic viscosity, $m^2 \cdot s^{-1}$
β	Coefficient of thermal expansion, K^{-1}
ρ	Gas density, $kg \cdot m^{-3}$
τ	Shear stress, $N \cdot m^{-2}$
k	Karman Constant

Abbreviations

UNEP	United Nations Environment Program
GWP	Global warming potential
SCPP	Solar chimney power plant
PCRs	Photocatalytic reactors
PPCR	Plate photocatalytic reactor
HPCR	Honeycomb photocatalytic reactor
ACW	Ambient crosswind

1. Introduction

Since the industrial revolution, the continuous increase in atmospheric CH$_4$ concentrations was caused by human beings. Despite the fact that the level of CH$_4$ in the atmosphere is substantially lower than that of CO$_2$ (1.886 ppm CH$_4$ vs 417 ppm CO$_2$), the damage caused by both is comparable [1]. The United Nations Environment Program (UNEP) had long stated that reducing CH$_4$ emissions could effectively slow

the high level of climate change, resulting in global temperature falling by 0.4 to 0.5°C

by 2050, which would aid in meeting the goal of the Paris Climate Agreement [2-4].

According to a recent report [5, 6], it was urgent to limit the increase of the CH_4

concentration in the atmosphere. The level of CH_4 was tightly connected to the rate of

global warming for two reasons. Firstly, CH_4 had a considerable radiative forcing

impact in a short period. For example, the warming capacity of CH_4 was 120 times than

CO_2 of the same mass, and its global warming potential (GWP) was 28-34 times higher

even after 100 years [7, 8]. Secondly, an increase in global temperatures would release

massive amounts of CH_4 locked as gas hydrate on the ocean bottom into the atmosphere,

aggravating the greenhouse effect even more [9]. If the atmospheric CH_4 level was

reduced to the pre-industrial level (0.76 ppm), a 16 % reduction in radiative forcing

could be accomplished in approximately 10-20 years [5, 10]. Furthermore, even if fossil

fuels were abandoned and no new CO_2 was released into the atmosphere, the existing

enormous carbon reservoir (513 Gt) of the atmosphere would continue to drive

temperature increase and climate change for several decades [11]. Therefore, reducing

atmospheric CH_4 is a promising solution to the climate change.

Thermal catalysis was the first suggested method for catalyzing rarefied CH_4, but

its applicability was restricted due to high energy consumption, low conversion rate,

and easy explosion [12]. Photocatalytic semiconductor technology was a mild and

manageable technique of degrading atmospheric CH_4 by employing solar energy, both

in terms of energy consumption, safety, and cost [13-15]. There was a dynamic balance

between the forward and reverse reactions in the thermocatalytic reaction, whereas, in

the photocatalytic reaction, the forward and reverse reaction mechanisms were different,

as was the energy. Hence, the photocatalytic reaction can break the thermodynamic

balance by eliminating the reverse reaction, which was beneficial to the degradation of

CH_4 [16]. Kato et al. [17] adopted Silica-Alumina as a photocatalyst to demonstrate the

non-oxidative coupling of CH_4 at room pressure and temperature for the first time,

however, the conversion rate was very low (5.9 %). The synthesis of new photocatalysts

contributed to the improvement of the selectivity and conversion of CH_4 photocatalytic

products. Wei et al. [18] reported a photocatalyst using Ga_2O_3 and Activated Carbon

(AC) at a mass ratio of 3:17 that performed well. Only CO_2 and H_2O were produced by CH_4 photocatalysis, and the catalytic rate was 91.5% after 2.5 h. Li et al. [19] used a hydrothermal approach to create ZnO nanosheets and nanorods with varying ratios of polar and non-polar crystal faces to focus on the degradation of low-concentration CH_4 (200ppm). The photocatalytic reaction of CH_4 on the ZnO surface followed quasi-first-order kinetics, with a degradation rate of 80% after 2h. Other photocatalysts, such as CuO/ZnO [20], Ag/ZnO [21], and $SrCO_3/SrTiO_3$ [22], also exhibited great promise in the degradation of low-concentration CH_4, with conversion rates of up to 100%. Brenneis et al. [23] accomplished all CH_4 removal by passing atmospheric level concentrations of CH_4 (2 ppm to 2%) through a reactor containing copper-treated zeolite particles heated to 310°C. Demonstration projects involving photocatalysis to degrade greenhouse gases were carried out [24-28], but the actual results were unsatisfactory because outdoor environmental factors such as solar radiation, wind speed and direction, and so on had a significant impact on the performance of photocatalysis [29].

The solar chimney power plant (SCPP), a green technology, was firstly proposed and built by Schlaich [30, 31], with a maximum power generation of 50 kW. To assess and forecast the performance of the SCPP, a wide range of internal heat transfer models were proposed [32-37]. Computational fluid dynamics (CFD) is a useful tool for numerical simulation of SCPP owing to the rapid advancement of computers. Koonsrisuk et al. [38-40] conducted CFD to investigate the effect of SCPP geometry on flow characteristics inside the system, and the findings revealed that a chimney with a certain divergence angle could improve the output power of the SCPP. Simulation results are more compatible with the actual data by using the radiation and solar load model in commercial software FLUENT [41]. However, due to the limitations of the SCPP prototype of the Spain, such as big floor space and high investment, researchers could only make tiny SCPP for testing. Zhou et al. [42] established a collector with a 10 m diameter and a chimney of 8 m height, and the temperature differential between the collector outlet and the surroundings reached 24.1°C. Kasaeian et al. [43] in the university of Zanjan built an SCPP. The collector was 10m in diameter, and the chimney

was 13 m in height, made of 12mm polyethylene tubing. The test data revealed that the collector had a substantial greenhouse effect, the outlet temperature was 25°C higher than the ambient temperature, and the maximum air speed was 3m/s. Ghalamchi et al. [44] built a small prototype to study the structural size formula of SCPP and the effect of different storage materials on system performance. Other small prototype trials [45-49] had also been recorded, demonstrating the potential of SCPP.

Innovative studies based on SCPP confirmed promising potential in air pollution purification, saltwater desalination, and crop drying [50, 51]. Cao et al. [52] presented a solar-assisted large-scale cleaning system (SALSCS) including a filter bank in the collector that could remove 22.4 km^3/day of urban air pollutants. It could significantly enhance urban air quality. De Richter et al. [53] launched a new concept of SCPP with photocatalytic reactors (SCPP-PCRs) for slowing global warming, where CH_4 was converted to CO_2 and H_2O as airflow moved over the surface of the photocatalyst in the atmosphere. One of the most important factors influencing the capacity of the SCPP-PCRs to degrade atmospheric CH_4 was the type of photocatalytic reactor, such as plate photocatalytic reactor (PPCR) and honeycomb photocatalytic reactor (HPCR) [54]. The reaction area of the HPCR was larger than that of the PPCR, but the pressure drop was higher and the reaction kinetic rate was slower [55, 56]. Ming et al. [57, 58] used a numerical method to examine the SCPP-PCRs. The atmospheric CH_4 of 21.31 kg per day was degraded, confirming the potential of the SCPP-HPCR for combating climate change. The PPCR just plated a layer of photocatalyst on the ground, with a less impact on the flow characteristics of the system. Another influencing factor was the ambient crosswind (ACW). Serag-eldin [59] briefly analyzed the influence of the ACW on SCPP using the CFD method. Zhou et al. [60] developed a theoretical model to quantitatively evaluate the influence of the ACW at the chimney outlet. Ming et al. [61] demonstrated that when the ACW was relatively weak, the flow field of the SCPP would deteriorate and the performance would degrade, but when the ACW was sufficiently strong, the performance would be improved dramatically. Placing a blockage close to the canopy entry or installing eight radial partition walls within the collector could significantly reduce the adverse impact of the ACW [62, 63].

The SCPP-PCRs is a negative emission technology. But research on it is still in its initial stage. Prior research on the SCPP-PCRs assumed that there was no ACW, but the system could not exist in isolation from the environment. It is uncertain how the ACW affects the performance of the photocatalytic CH_4 and power generation after the installation of the HPCR or PPCR. In this paper, the influences of the ACW on the overall performance of the SCPP-PCRs were analyzed by three-dimensional numerical simulation. This work will help to guide the design and building of the SCPP-PCRs prototype, providing a technical solution for quick and large-scale greenhouse gas removal.

2. Model and method

2.1 Geometric model

The geometric model is determined by simplifying the SCPP Manzanares Prototype in this work [64]. The chimney is 200 m in tall and 10 m in diameter. The collector height increases from 2 m at the entrance to 6 m at the center linearly. And collector diameter is 240 m. Setting acceptable boundary conditions, the performance of SCPP-PCRs in large space can be analyzed by locating the model in the middle of a non-existent box with X, Y, and Z directions of 400 m, 400 m, and 300 m, respectively [61]. Because the model is symmetric at the XZ plane, halving the computational domain, as shown in Fig. 1, does not affect calculation accuracy.
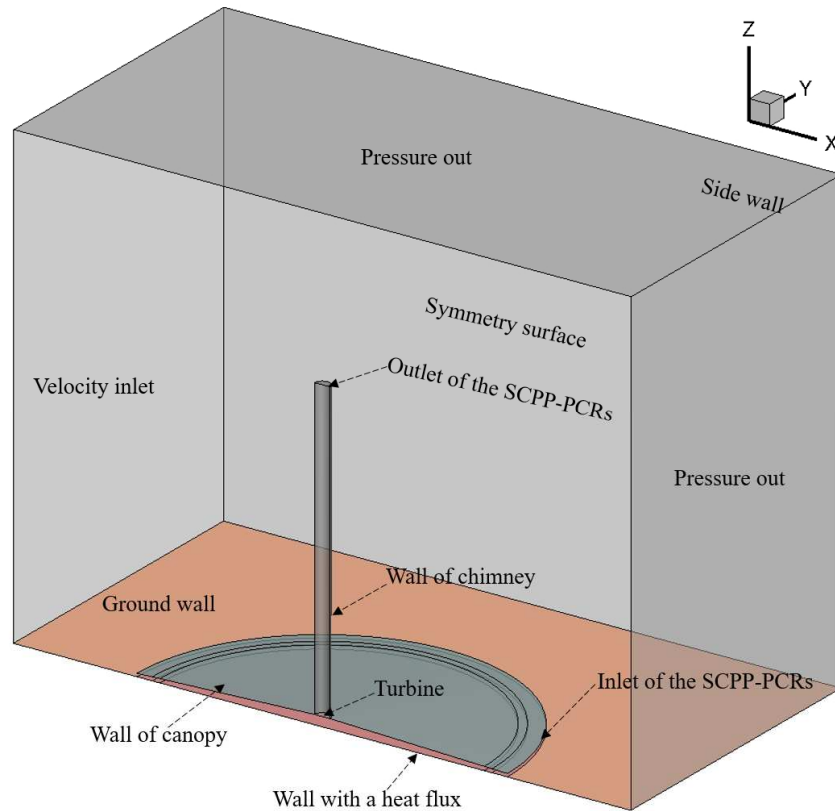
Fig. 1 Schematics of the geometrical model

The HPCR is located 10 m from the entrance of the canopy and is 5 m in length, filling the flow channel of the canopy. As indicated in Fig. 2(a), the photocatalyst (P25) is evenly coated on the inner surface of the honeycomb channel. The honeycomb internal channels are in parallel with the airflow, resulting in relatively low pressure drop. Meanwhile, for the PPCR as shown in Fig. 2(b), the photocatalyst (P25) is uniformly painted on the ground under the collector. The inner environment of SCPP is under negative pressure due to the buoyancy effect caused by solar radiation, thereby, CH_4 in the atmosphere is continually drawn into the system and is converted to CO_2 and H_2O when exposed to the photocatalyst.
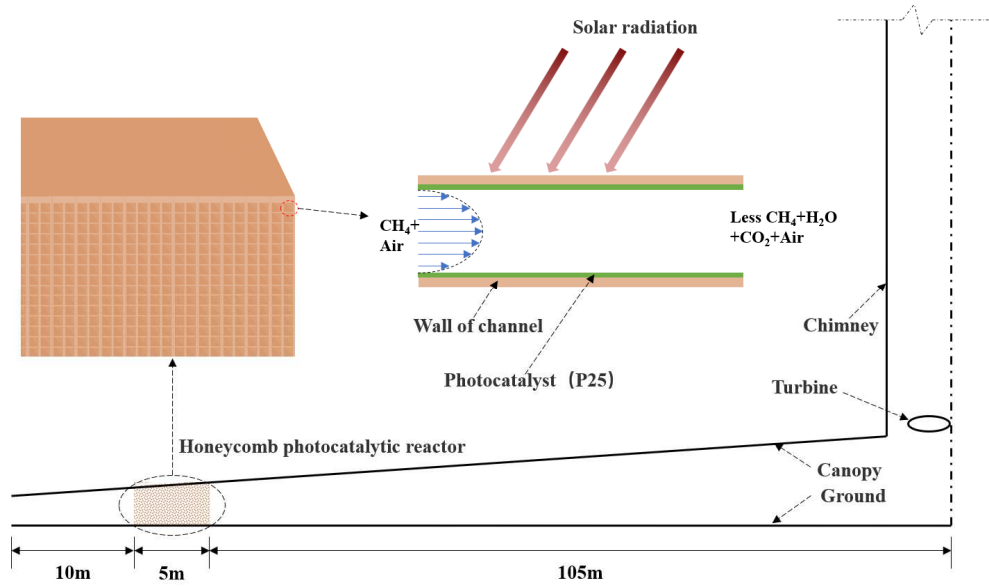
(a)
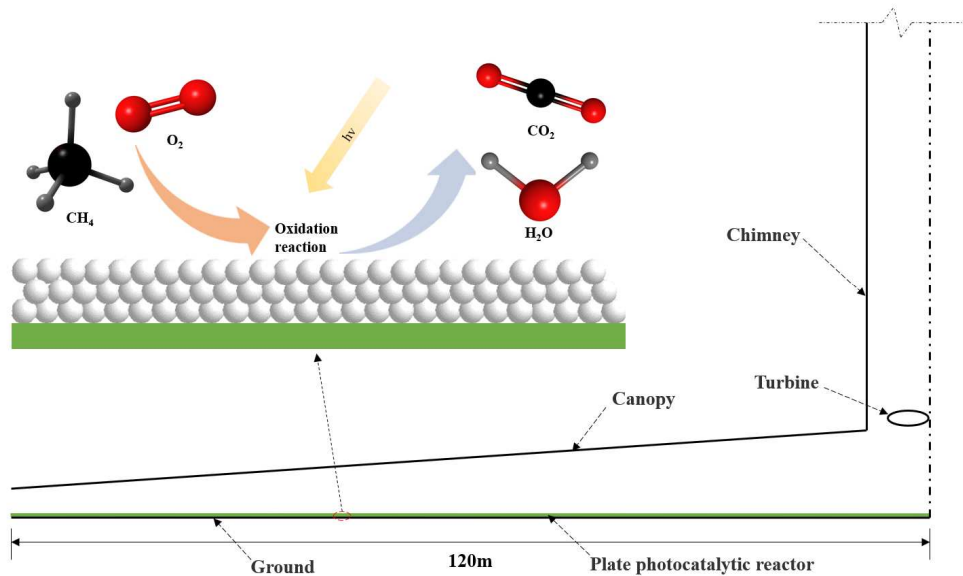
(b)

Fig. 2 Schematics of the SCPP-PCRs: (a) SCPP-HPCR; (b) SCPP-PPCR.

2.2 Numerical model

The flow inside the system is driven by the natural convection caused by the solar radiation heating the ground. The Rayleigh number can be used as a criterion to measure the buoyancy force, which is defined by:

$$R_a = \frac{g\beta\Delta T H^3}{av} \tag{1}$$

where ΔT is the maximum temperature rise in the SCPP-PCRs. g, β, a, and H are the gravitational acceleration (9.81 m²/s), the thermal expansion coefficient, the thermal

8

166   diffusivity, and the collector height, respectively. The system is in a turbulent state as

167    $R_a > 10^{10}$ [61].

168   The incompressible ideal gas model is used to model the gas density variation in

169   the SCPP-PCRs [65]. The macroscopical process of CH4 photocatalytic reaction is

170   simulated using the laminar finite rate model. The governing equations of the flow and

171   chemical reactions in the SCPP-PCRs are given as follows.

172   Continuity equation:

173
$$\frac{\partial(\rho u_i)}{\partial x_i} = 0 \tag{2}$$

174   Momentum equation:

175
$$\frac{\partial(\rho u_i u_j)}{\partial x} = \rho g_i - \frac{\partial p}{\partial x_i} + \frac{\partial \tau_{ij}}{\partial x_j} \tag{3}$$

176   Energy equation:

177
$$\frac{\partial(\rho c_p u_j T)}{\partial x_j} = \frac{\partial}{\partial x_j}\left(\lambda \frac{\partial T}{\partial x_j}\right) + \tau_{ij}\frac{\partial u_i}{\partial x_j} + \beta T \left(\frac{\partial p}{\partial t} + u_j \frac{\partial p}{\partial x_j}\right) \tag{4}$$

178   Equation for the turbulent kinetic energy (k):

179
$$\frac{\partial}{\partial x_i}(\rho k u_i) = \frac{\partial}{\partial x_j}\left(\alpha_k \mu_{eff}\frac{\partial k}{\partial x_j}\right) + G_k + G_b - \rho\varepsilon - Y_M + S_k \tag{5}$$

180   Equation for the energy dissipation (ε):

181
$$\frac{\partial}{\partial x_i}(\rho\varepsilon u_i) = \frac{\partial}{\partial x_j}\left(\alpha_\varepsilon \mu_{eff}\frac{\partial\varepsilon}{\partial x_j}\right) + C_{1\varepsilon}\frac{\varepsilon}{k}(G_k + C_{3\varepsilon}G_b) - C_{2\varepsilon}\rho\frac{\varepsilon^2}{k} - R_\varepsilon + S_\varepsilon \tag{6}$$

182   Component transport equation:

183
$$\nabla \cdot (\rho\vec{v}Y_i) = -\nabla \cdot \vec{J_i} + R_i + S_i \tag{7}$$

184   where μ_{eff} denotes the effective kinematic viscosity, $\mu_{eff} = \mu + \mu_t$. τ_{ij} is the

185   viscous shear stress, which is $\tau_{ij} = \mu\left(\frac{\partial u_i}{\partial x_j} + \frac{\partial u_j}{\partial x_i}\right)$. G_k represents the generation of

186   turbulence kinetic energy owing to buoyancy, which is defined as $G_k = -\rho\overline{u_i' u_j'}\frac{\partial u_j}{\partial x_i}$,

187   α_k and α_ε are the turbulent Prandtl numbers for k and ε respectively. $\alpha_k = \alpha_\varepsilon =$

188   1.30. $C_{1\varepsilon}$ and $C_{2\varepsilon}$ are two constants for the turbulent model, with $C_{1\varepsilon} =$

189   1.44, $C_{2\varepsilon} = 1.92$. $\vec{J_i}$ represents the diffusion flux of species i, $\vec{J_i} = -\rho D_{i,m} + R_i$.

190   R_i represents the amount of component i produced or consumed in a chemical

191   reaction. S_i represents the additional rate owing to the discrete phase. Y_M indicates

192   the variable dilatation incompressible turbulence contribution to the total dissipation

193 rate.

194 A two-dimensional reverse fan model [66] with a preset pressure drop could

195 calculate the output power of the SCPP-PCRs, with the formula given as follows [67].

$$W_e = \eta_t \cdot \Delta P \cdot V \qquad (8)$$

197 where η_t represents the efficiency of the SCPP-PCRs to convert heat energy into

198 electricity (0.72). ΔP represents a pressure drop. V represents the volume flow rate

199 at the outlet of the SCPP-PCRs.

200 The reaction rate of CH4 in the plate reactor is given by [68]

$$r_{AI} = B \frac{B_1 c_1}{1+B_1 c_1} \frac{B_2 c_2}{1+B_2 c_2} \qquad (9)$$

202 where c_1 and c_2 are the concentration of CH4 and O2, respectively. B, B_1 and B_2 are

203 the associate parameters, whose values are 5.37×10^{-7}, 2.42, and 4.60, respectively.

204 The honeycomb reactor is simplified as a porous media. The governing equations

205 inside the porous media are presented as follows.

206 *Continuity equation:*

$$\nabla \cdot (\gamma \rho \vec{v}) = 0 \qquad (10)$$

208 *Momentum equation:*

$$\nabla \cdot (\gamma \rho \vec{v}) = -\gamma \nabla p(\gamma \bar{\tau}) + \gamma \rho \vec{g} + S_\Phi \qquad (11)$$

210 where γ is porosity ($\gamma = 0.85$), $\bar{\tau}$ represents the viscous stress tensor, S_Φ denotes the

211 momentum loss term, $S_\Phi = -(\frac{\mu}{K}\vec{v} + \frac{C}{2}\rho|\vec{v}|\vec{v})$. The permeability (K) and the inertia

212 coefficient (C) can be calculated by the Ergun equations [69]:

$$K = \frac{D_P^2}{150} \frac{\gamma^3}{(1-\gamma)^2} \qquad (12)$$

$$C = \frac{3.5}{D_P^2} \frac{(1-\gamma)}{\gamma^3} \qquad (13)$$

215 where D_P is the pore diameter.

216 The reaction rate of CH4 in the honeycomb reactor is given by

$$r_m = r_{AI} \cdot SSA \qquad (14)$$

218 where SSA is the specific surface area, $SSA = \frac{6(1-\gamma)}{D_P}$ [57].

219 The purification rate of CH4 is given by Eq. (15).

$$\dot{m}_{CH_4} = Q_m(m_1 - m_2) \qquad (15)$$

221 where Q_m represents the mass flow rate of the system, m_1 and m_2 are the mass

10

222 fractions of CH$_4$ at the entrance and exit of the reactor, respectively.

223

224 *2.3 Boundary conditions*

225   Fig.1 shows the boundary conditions and coordinate directions of the model, and

226 the details are listed in Table 1.

227 <div align="center">Table 1 Boundary conditions</div>

Name and location	Type	Value
Inlet (X = -200 m)	Velocity inlet	$u = \frac{1}{\kappa} \cdot (\frac{\tau_s}{\rho})^{\frac{1}{2}} \cdot ln \frac{z}{z_0}$
Outlet (X = 200 m and Z = 300 m)	Pressure outlet	$P = 0$ Pa, $T = 293$ K
Ground below the collector (Z = 0 m)	Heat flux	$q = 600$ W/m^2
Ground beyond the collector (Z = 0 m)	Temperature	$T = 318$ K
Side wall (Y = 200 m)	Wall	$q = 0$ W/m^2
Chimney	Wall	$q = 0$ W/m^2
Turbine	Fan	$\triangle P = 0 \sim 440$ Pa
Canopy	Coupling	Exterior surface: $\lambda \left(\frac{\partial T}{\partial x}\right) = \alpha\left(T_f - T_w\right)$ Interior surface: $\lambda \left(\frac{\partial T}{\partial x}\right) = \alpha\left(T_w - T_f\right)$
Symmetry (Y = 0 m)	Symmetry	$\frac{\partial \varepsilon}{\partial n} = 0$

228   Assuming that the ACW measurement at the entrance is completely developed and

229 that the temperature remains constant at 293 K, the wind speed equation at the inlet (X

230 = -200 m) can be fitted using the logarithmic law of atmospheric boundary layer wind

231 speed profile [70]:

232 $$v = w = 0 \tag{16}$$

233 $$u = \frac{1}{\kappa} \cdot (\frac{\tau_s}{\rho})^{\frac{1}{2}} \cdot ln \frac{z}{z_0} \tag{17}$$

234 where τ_s is the shear stress on ground surface. z_0 is the aerodynamic roughness

235 length of the ground. κ and z_0 are 0.4 and 0.01, respectively [61].

236   The ground absorbs solar energy, accounting for 70% of the total amount [61].

237   When the solar radiation is 857 W/m^2, the heat flux of the ground below the collector

238   is about 600 W/m^2, and other regions are supposed to have a constant temperature

239   boundary (318 K) [62]. The surfaces at X = 200 m and Z = 300 m are two pressure

240   outlets, which are set far enough to ensure the flow field develops fully. The side wall

241   is far from the inlet and outlet of the SCPP-PCRs, therefore the default side wall

242   characteristic parameters are so preserved [62]. The canopy and chimney are set as

243   thermal coupling wall and insulation wall, respectively, and their thickness are

244   neglected.

245

246   *2.4 Grid system and computational processes*

247   In the process of numerical simulation, the structured grid is more stable and

248   economical than unstructured grid. A hexahedral grid system is used in the model and

249   the generation procedure is carried out with the commercial software ICEM CFD 19.2,

250   as shown in Fig. 3. The SCPP with different photocatalytic reactors employs the same

251   grid system by densifying the grids in the area 10 ~ 15 m away from the entrance of the

252   collector. The common fluid region is set for the PPCR and the porous media model is

253   used to simulate the HPCR in this area. Ansys Fluent 19.2 is adopted in the

254   computational procedure. The SIMPLE algorithm is selected for the pressure–velocity

255   coupling scheme. For the pressure term, the PRESTO! divergence scheme is utilized,

256   while the other terms are calculated using the second order upwind scheme. The

257   maximum residuals of all equations are below 10^{-5}. The concentration of CH_4 and the

258   volume flow rate at the chimney outlet remain constant as the criterion for calculating

259   convergence.
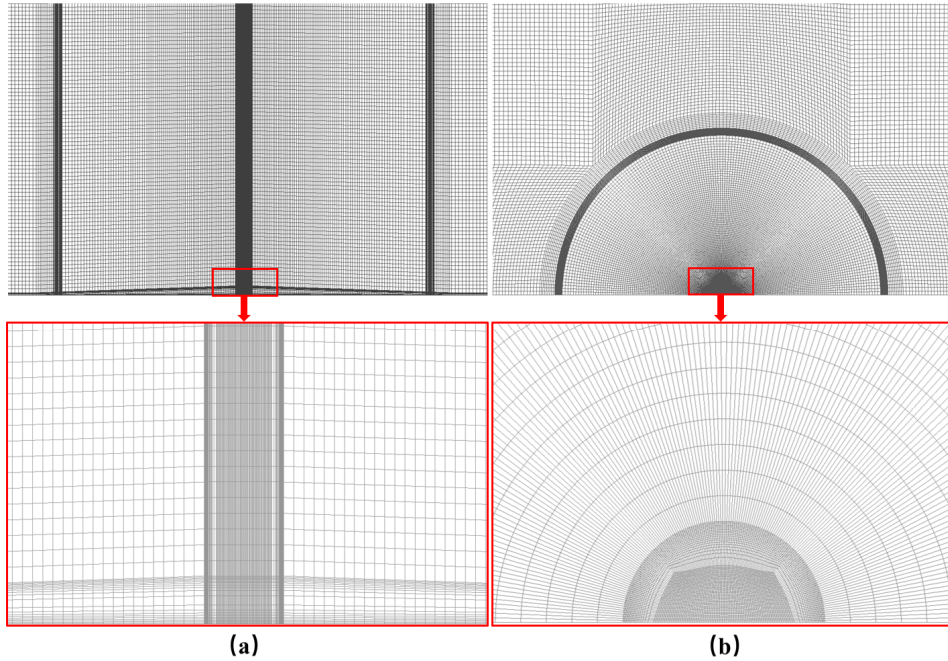
261   Fig. 3 Grid system of the SCPP-PCRs: (a) grid distribution on the symmetric surface;

262   (b) Top view of grid distribution.

263   Three grid systems with grid numbers of 4,575,628, 5,185,508, and 6,458,736,

264   respectively, are adopted to investigate grid independence. The numerical simulations

265   are carried out in the same conditions (ACW = 0 m/s, $G = 857$ W/m^2, and $\triangle P = 0$ Pa).

266   As shown in Fig. 4, The maximum deviation of the average velocity of the chimney

267   outlet is less than 2.32%. Therefore, the simulations are thought grid independent. And

268   the grid system with a grid number of 5,185,508 is adopted for the modeling.
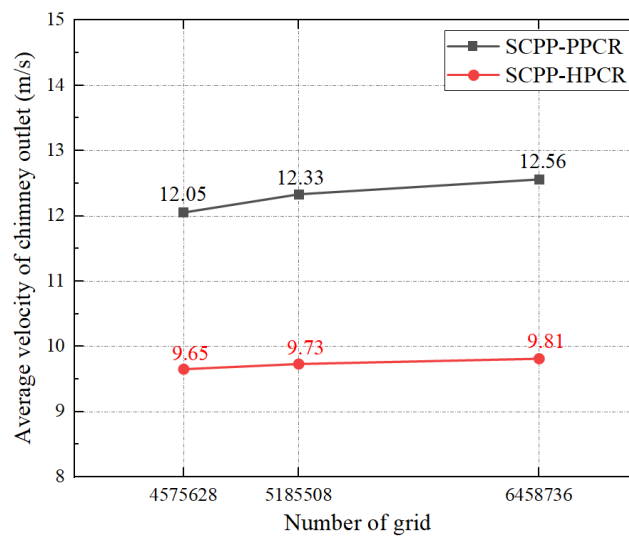
269

270   Fig. 4 Grid independence check

2.5 Simulation validation

For SCPP-PPCR, because the PPCR has minimum affect on the flow of the SCPP, the results are compared with the data in reference [71] to confirm the validity of the simulation. The outlet velocity of SCPP-PPCR is 12.33 m/s while that of SCPP is 12.61 m/s when ACW = 0 m/s, G = 857 W/m^2, and $\triangle P$ = 0 Pa. The relative error is 2.22%. For SCPP-HPCR, according to reference [57], the outlet velocity of SCPP-HPCR is 9.38 m/s and the purification rate of CH_4 is 0.59 g/s while that of the simulation result are 9.73 m/s and 0.55 g/s when ACW = 0 m/s, G = 857 W/m^2, and $\triangle P$ = 0 Pa. The maximum relative error is 6.78%. As a result, the validation of the simulation is demonstrated as the modeling result matches well with the experimental result.

3. Result and analysis

In this section, a series of the ACWs ($U_{200\,m}$) ranging from 0 to 25 m/s by intervals of 5 m/s were adopted to simulate the effect of the ACW on the performance of the system. The output power of the system was calculated based on the preset turbine pressure drops and the corresponding flow rates [72]. The HPCR was treated as a porous medium with a porosity of 0.85 and a pore size of 4 mm. In addition, the difference in the overall performances of SCPP-PCRs were analyzed under no-load condition.

3.1 Flow characteristics of the SCPP-PCRs

Fig.5 and 6 showed the contours of velocity in the XZ plane (Y = 0 m) of the SCPP-PCRs under G = 857 W/m^2. Fig. 5 and 6(a), (c), and (e) demonstrated the flow fields of the SCPP with plate photocatalytic reactor (SCPP-PPCR), while Fig.5 and 6(b), (d), and (f) were the results of the SCPP with honeycomb photocatalytic reactor (SCPP-HPCR). The ACWs were preset to 0 m/s, 10 m/s, and 20 m/s, respectively. As shown in Fig.5 and 6, the velocity distribution in the two systems were generally symmetrical when ACW = 0 m/s. The SCPP-PPCR had a flow velocity that was higher than the SCPP-HPCR due to the flow resistance caused by the honeycomb reactor.

As shown in Fig.5 and 6, the HPCR could reduce the impact of the ACWs on the flow in the system. Although the ACW varies, the flow velocity in the SCPP-HPCR

were drastically decreased (close to 0 m/s) when the ACW entered the porous material. However, the flow field of the SCPP-PPCR in the collector was significantly impacted by the ACW. The wind coming from the left side of the collector was divided into two streams at the bottom of the chimney, with one flowing into the chimney and another slipping into the right side of the collector.
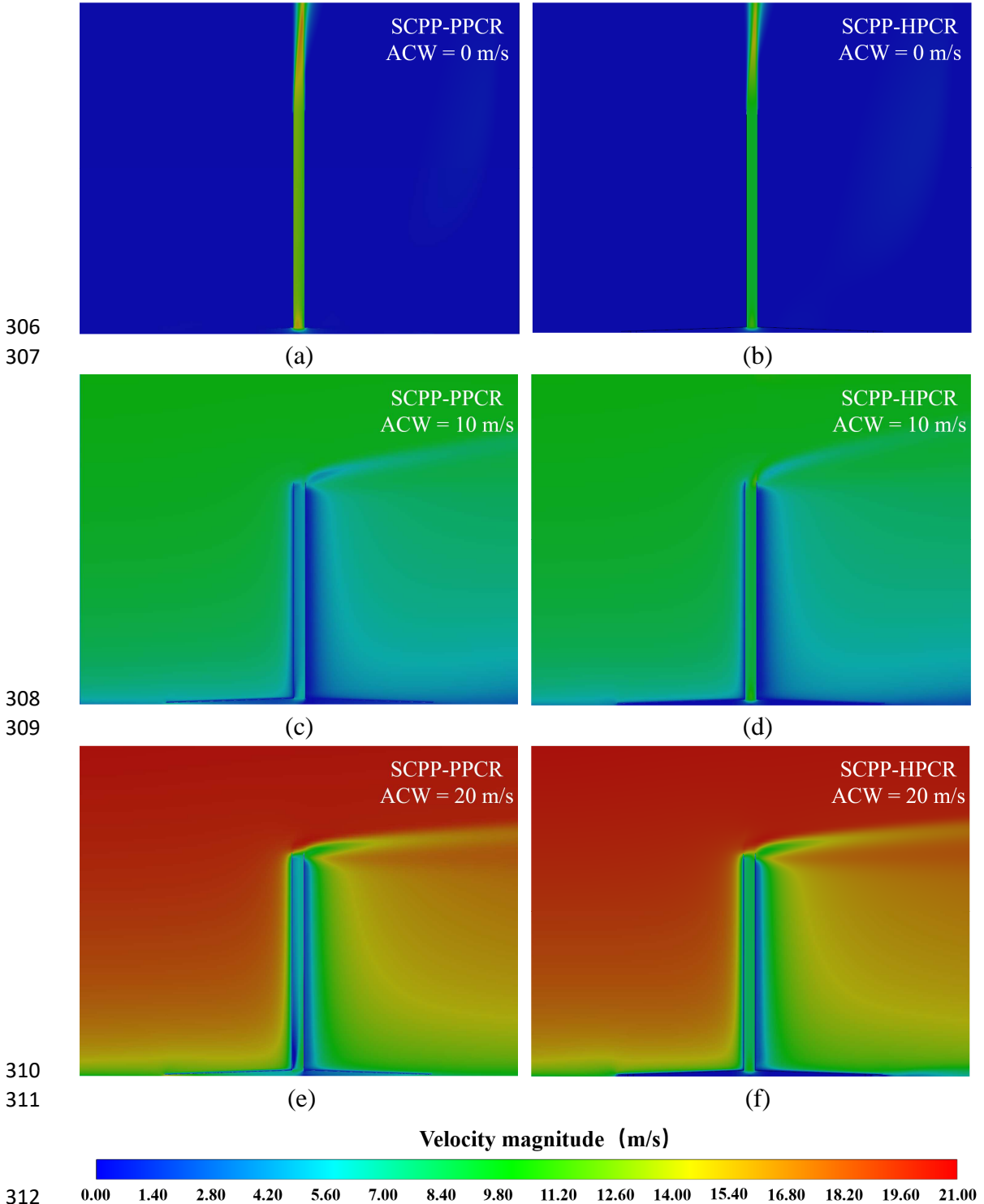

(a) (b)
(c) (d)
(e) (f)

Velocity magnitude（m/s）

0.00 1.40 2.80 4.20 5.60 7.00 8.40 9.80 11.20 12.60 14.00 15.40 16.80 18.20 19.60 21.00

Fig.5. The velocity contours in the XZ plane (Y = 0 m) of the SCPP-PCRs under

15

ACWs = 0, 10, 20 m/s at G = 857 W/m^2.

(a)

(b)

(c)

(d)

(e)

(f)
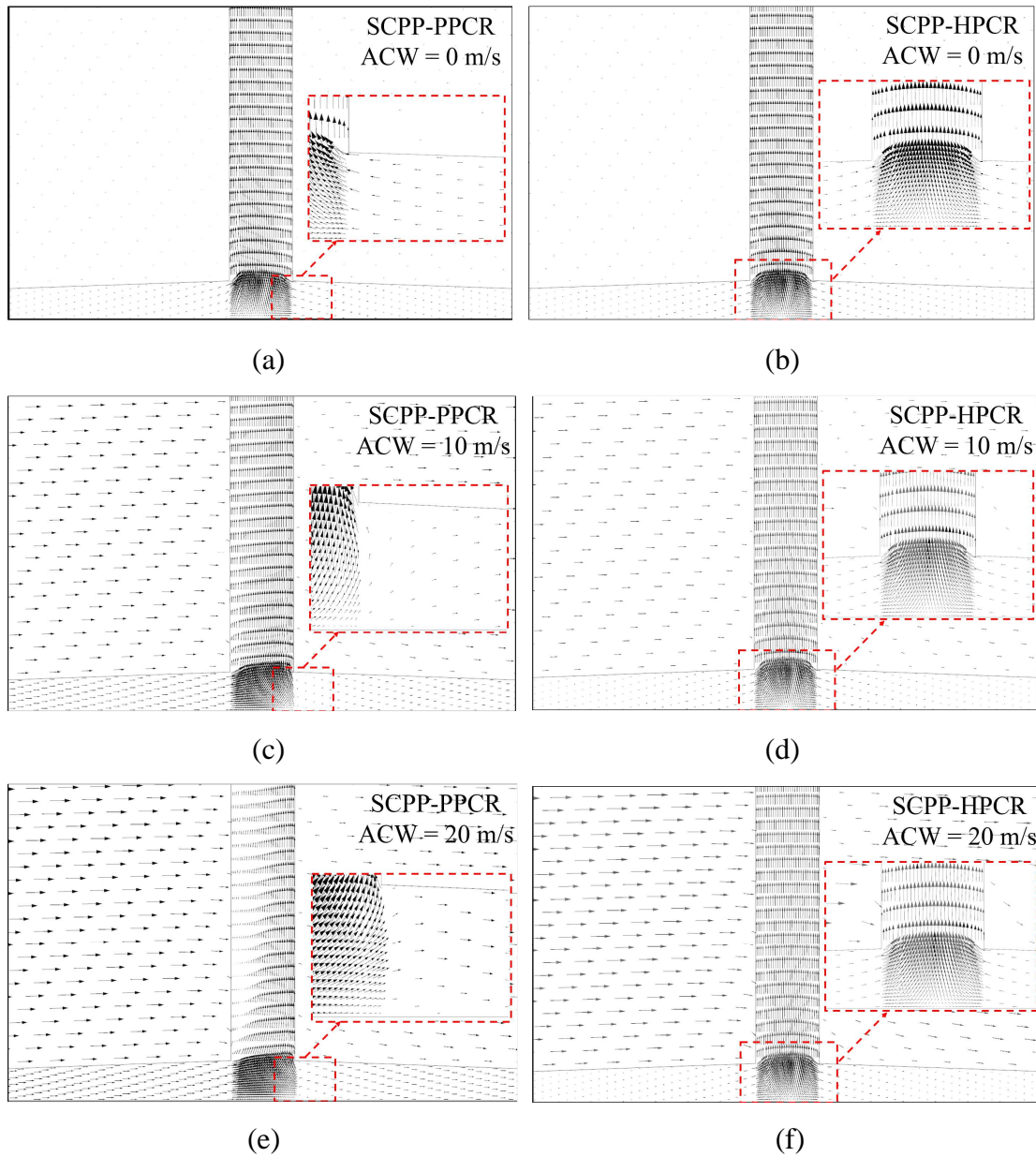
Fig.6. The velocity vectors at the bottom of the SCPP-PCRs under ACWs = 0, 10, 20 m/s at G = 857 W/m^2.

Fig.7 showed the average velocity of the chimney outlet of the SCPP-PCRs at G = 857 W/m^2. The outlet velocity of the two systems fluctuated abiding by the same change law, which saw a fall followed by a rise, but the fluctuation ranges differ. When the ACW was weak, the airflow in the collector was collected at the bottom of the chimney. As the porous medium increased the flow resistance, the outlet velocity of the SCPP-PPCR decreased significantly. When ACW = 0 m/s, the outlet velocity of the

331   SCPP-PPCR was 12.33 m/s, while the SCPP-HPCR was only 9.73 m/s. When ACW

332   was larger than 10 m/s, the outlet velocity of the SCPP-PPCR was rapidly decreased

333   due to the enthalpy loss of hot air, which was consistent with the analysis of Serag-

334   Eldin [59]. The outlet velocity of the SCPP-HPCR was slightly reduced due to the

335   resistance of the porous medium, but much higher than that of the SCPP-PPCR. The

336   high-speed air flow at the chimney outlet created a negative pressure zone and

337   strengthens the driving force of the system as the ACW further improves. When the

338   ACW = 15 m/s, the outlet velocity of the SCPP-HPCR reached 9.74 m/s which

339   exceeded that of the ACW = 0 m/s. However, too high ACW could result in forced

340   vibration and static dynamic instability, which could damage the chimney's

341   construction and increase the risk of accidents [73].
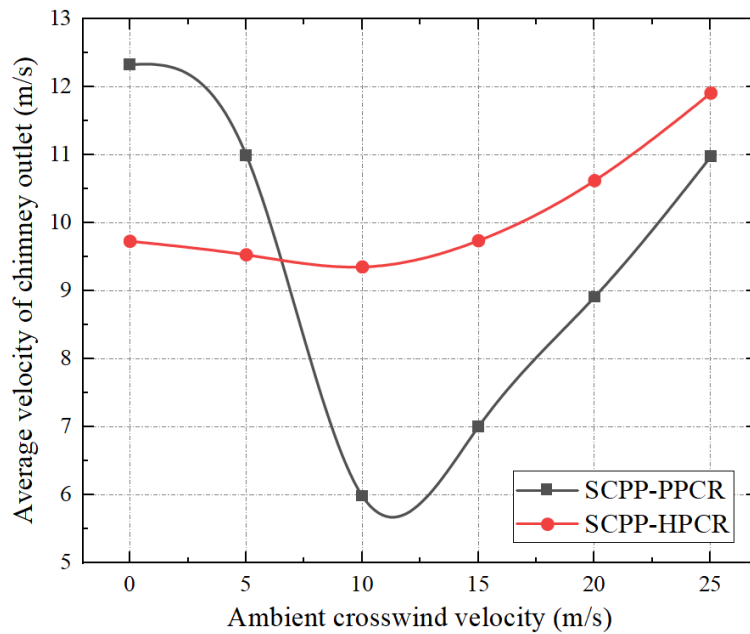
342

343   Fig.7. The average velocity of chimney outlet of the SCPP-PCRs at $G = 857$ W/m^2.

344

345

346   *3.2 Distribution of CH$_4$ in the SCPP-PCRs*

347   Fig.8 showed concentration contours of CH$_4$ in the XZ plane (Z = 0.01m) of the

348   SCPPs at $G = 857$ W/m^2. When the ACW was weak, atmospheric CH$_4$ entered the

349   system through the collector inlet. Then it was degraded in the reactor. And finally the

350   cleaned air was emitted from the chimney outlet. The stronger the ACW, the faster the

351   CH$_4$ mixed with the environment at the outlet. In addition, part of atmospheric CH$_4$

entered the SCPP-PPCR through the entry on the left side of the collector, and flowed

into the chimney along the collector without reacting when the ACW was too large (20

m/s) as shown in Fig.9(e). For the SCPP-HPCR, the distribution of CH_4 in the system

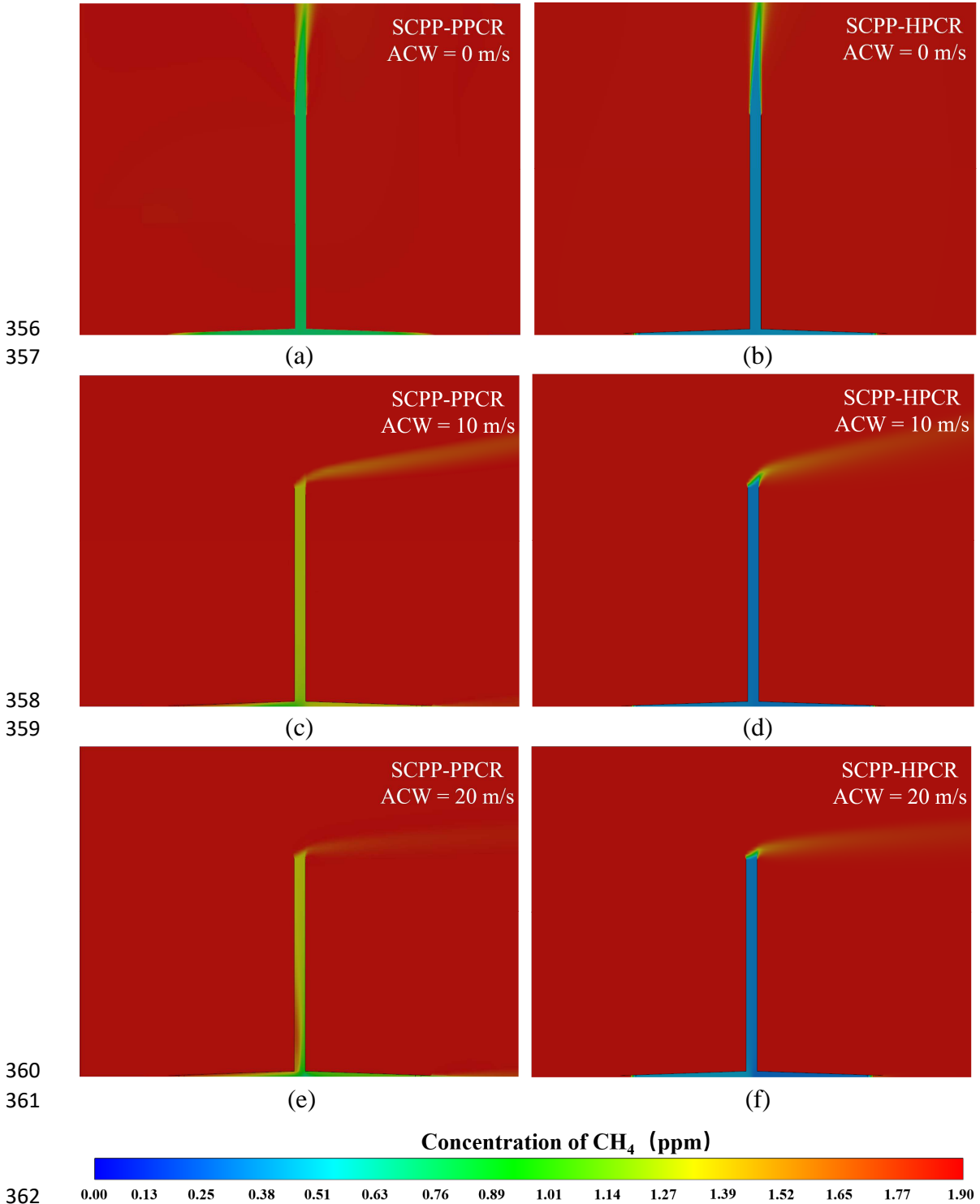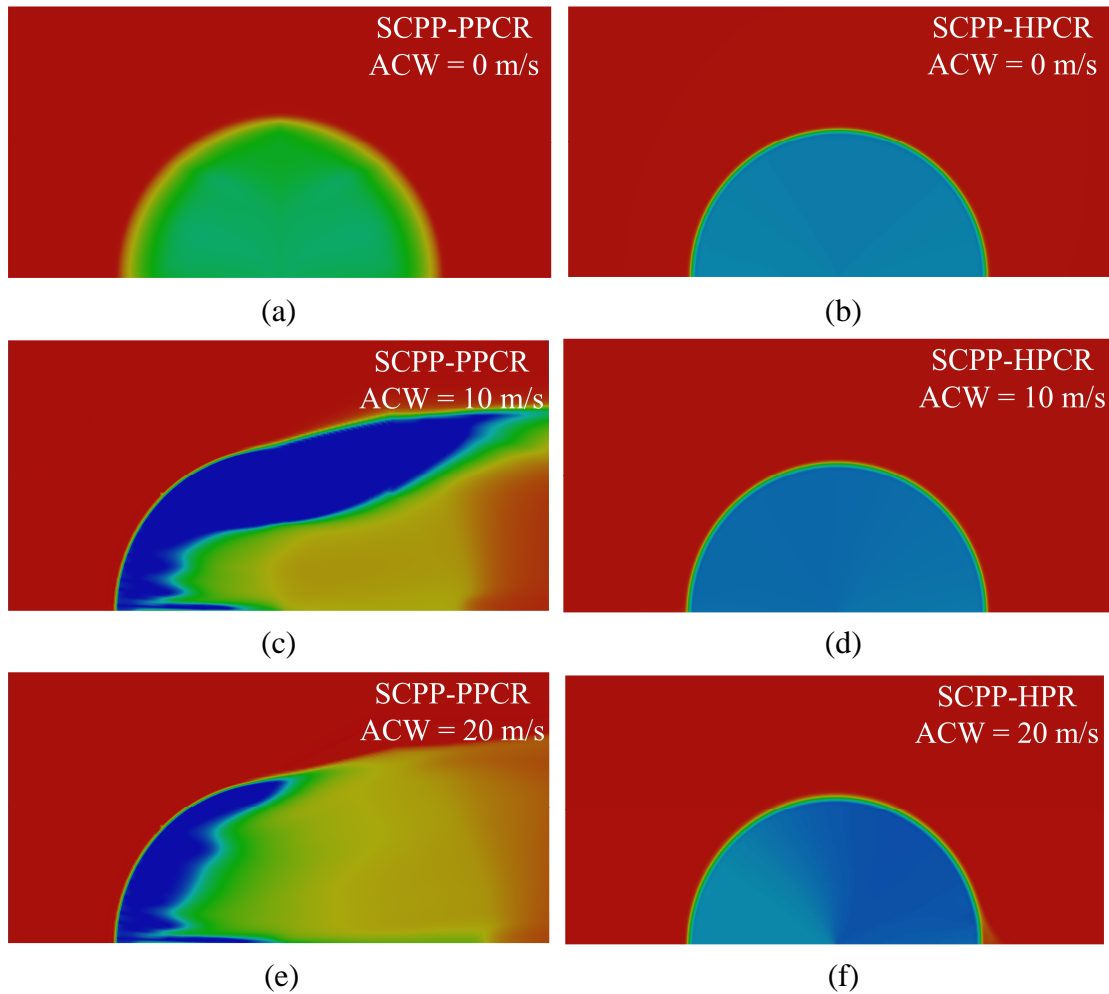was much more uniform and the concentration was lower than that of the SCPP-PPCR.

(a)

(b)

(c)

(d)

(e)

(f)

Concentration of CH_4 (ppm)

0.00   0.13   0.25   0.38   0.51   0.63   0.76   0.89   1.01   1.14   1.27   1.39   1.52   1.65   1.77   1.90

Fig.8. The contours of CH_4 in the XZ plane (Y = 0 m) of the SCPP-PCRs under
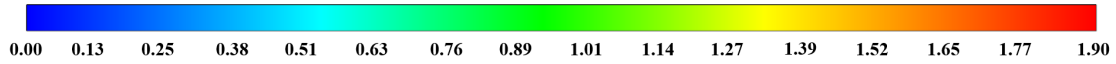ACWs = 0, 10, 20 m/s at G = 857 W/m^2.

Fig.9 displayed the concentration contours of CH_4 in the XY plane (Z = 0.01 m) of the SCPP-PCRs at G = 857 W/m^2. For the SCPP-HPCR, there was a relatively large concentration gradient in the airflow direction as a result of the fast reaction rate in the PPCR. CH_4 escaped to the right from the collector as the ACW continued to strengthen. For the SCPP-HPCR, the concentration of CH_4 decreased in the direction of the reactor when the ACW was weak because it was only degraded in the honeycomb tunnel. The CH_4 in the collector within the reactor was evenly distributed when the ACW was weak. When ACW = 20 m/s, the CH_4 concentration in the collector was lower on the left, because a slight leakage of CH_4 occurred at the right inlet of the collector. In general, the removal of atmospheric CH_4 utilizing SCPP-HPCR was easier to control in response to the ACW.

(a)   (b)

(c)   (d)

(e)   (f)

Concentration of CH$_4$ （ppm）

| 0.00 | 0.13 | 0.25 | 0.38 | 0.51 | 0.63 | 0.76 | 0.89 | 1.01 | 1.14 | 1.27 | 1.39 | 1.52 | 1.65 | 1.77 | 1.90 |

Fig.9. The distribution of CH$_4$ in the XY plane (Z = 0.01 m) of the SCPPs under ACWs = 0, 10, 20 m/s at G = 857 W/m^2.

Fig.10 displayed the concentration contours of CH$_4$ in the chimney outlet of the SCPP-PCRs at G = 857 W/m^2. The weak ACW inhibited the updraft at the chimney outlet of the SCPP-PPCR [61], resulting in slower airflow and a longer time for CH$_4$ to react when the ACW = 5 m/s. As a result, the concentration of CH$_4$ at the outlet decreased. When ACW was strong, atmospheric CH$_4$ entered the chimney along the collector's interior wall without reacting. Additionally, an amount of cleaned air was to escape out of the right side of the collector, resulting in a high concentration of CH$_4$ at the outlet of the chimney. The concentration of CH$_4$ at the exit for the SCPP-HPCR rose linearly with the ACW, and it was lower than the SCPP-PPCR. The CH$_4$ concentration of the outlet at 757.51 ppb was roughly half that of the SCPP-PPCR when the ACW = 25 m/s.
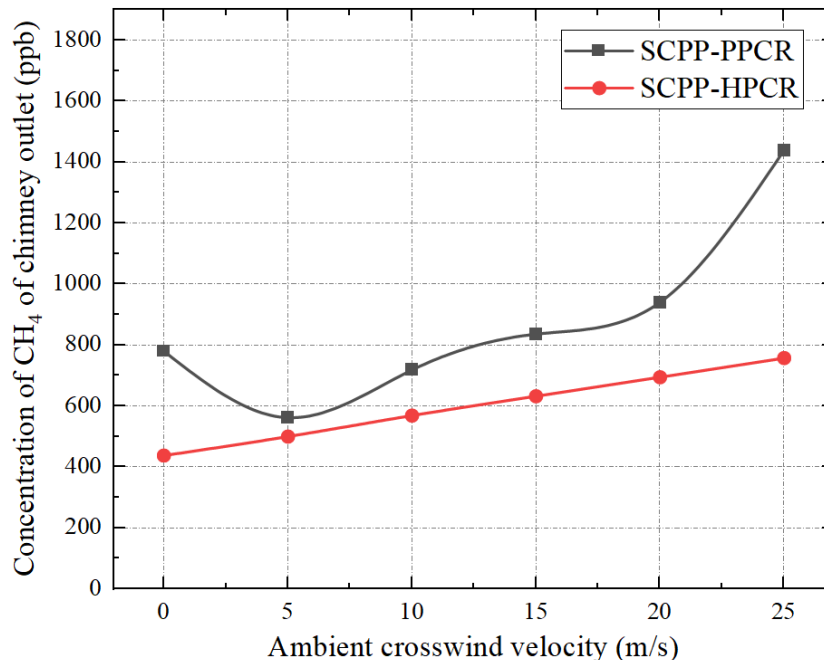
Fig.10. The concentration of CH$_4$ in the chimney outlet of the SCPP-PCRs at G = 857 W/m^2.

3.3 Performance of methane degradation

404   Fig.11 displayed the CH_4 purification rate of the SCPP-PCRs at $G = 857$ W/m^2.

405   The purification rate of CH_4 for the two systems steadily dropped with an increase in

406   ACW, eventually approaching a constant value. As seen in Fig. 7 and Fig.10, when the

407   ACW = 0 m/s, the SCPP-PPCR had a higher outlet flow rate than the SCPP-HPP, but

408   the concentration of CH_4 was higher. However, the purification rate of CH_4 of the

409   SCPP-PPCR at 0.89 g/s was higher than the SCPP-HPCR of 0.54 g/s as demonstrated

410   in Fig.11. Therefore, the flow rate of the outlet of the system was extremely important

411   for the purification rate of CH_4. When the ACW = 10 m/s, the SCPP-PPCR tend to

412   purify CH_4 at a rate of 0.11 g/s that did not drop when ACW increases, but the SCPP-

413   HPCR was 0.41 g/s under the ACW = 25 m/s.
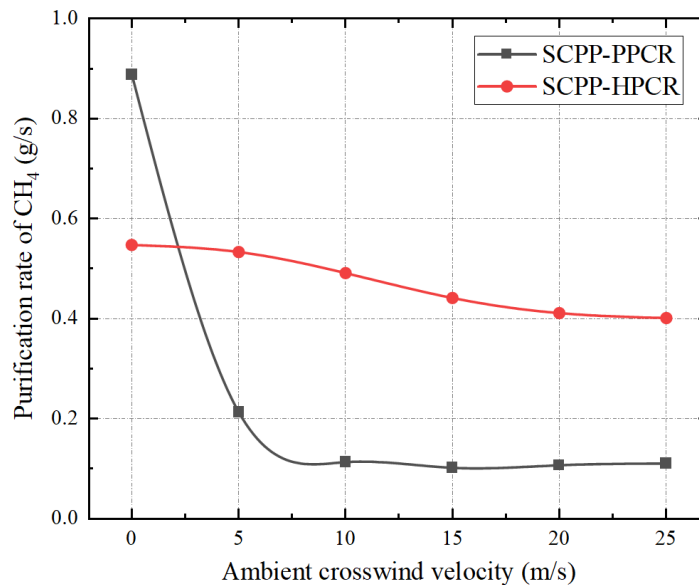
414

415   Fig.11. The CH_4 purification rate of the SCPP-PCRs at $G = 857$ W/m^2.

416

417   It was found that the SCPP-HPCR was better at purifying atmospheric CH_4 than

418   the SCPP-PPCR. The association between the purification rate of CH_4 and turbine

419   pressure drop of the SCPP-HPCR was discussed.

420   Fig. 12 displayed the CH_4 degradation performance of the SCPP-HPCR at $G =$

421   857 W/m^2. More kinetic energy from the thermal flow in the system was turned into the

422   mechanical energy of the turbine. The output power of the turbine could increase, but

423   the mass flow rate of the system was significantly decreased. The purification rate of

424   CH_4 was greatly influenced by the mass flow rate of the system, hence purification rate

425 fell as the pressure drop of the turbine increased. It was worth noting that the downward

426 trend of CH_4 purification rate became slow when the ACW = 20 and 25 m/s. The

427 purification rate was higher than in the case of relatively weak ACW as turbine pressure

428 drop increased. This was due to the outlet velocity of the chimney was higher at the

429 ACW = 20 and 25 m/s, as shown in Fig. 7.

430   Fig. 13 displayed the concentration of CH_4 in the outlet of the SCPP-HPCR at G

431 $= 857$ W/m^2. When the pressure drop of the turbine increased, the concentration of CH_4

432 at the chimney outlet could reach a minimal value, but the stronger the ACW, the higher

433 the CH_4 concentration at the chimney outlet. For example, the level of CH_4 at the

434 chimney outlet was 247.49 ppb when the ACW = 0 m/s and the $\triangle P = 400$ Pa, but the

435 level of CH_4 was 754.47 ppb when the ACW = 25 m/s and the $\triangle P = 60$ Pa.
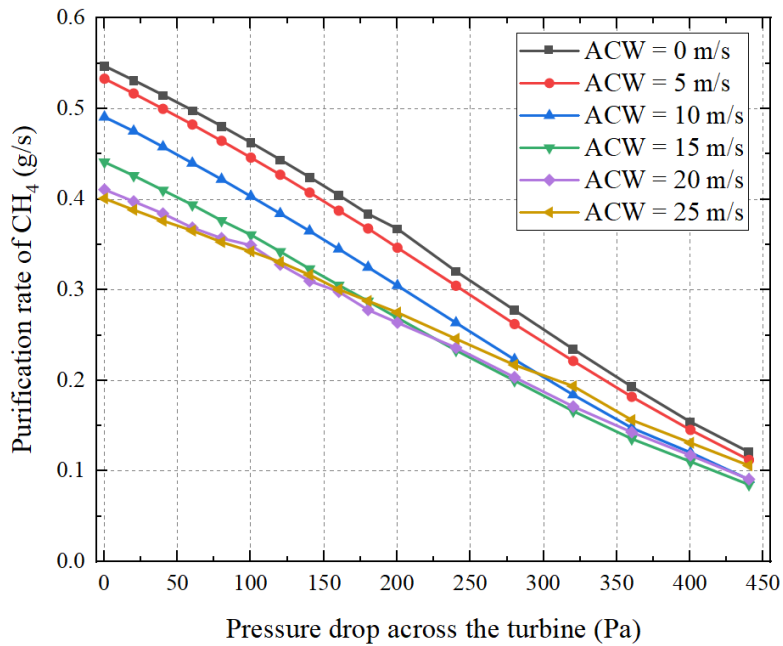
436

437   Fig.12. The performance of CH_4 degradation of the SCPP-HPCR at $G = 857$ W/m^2.
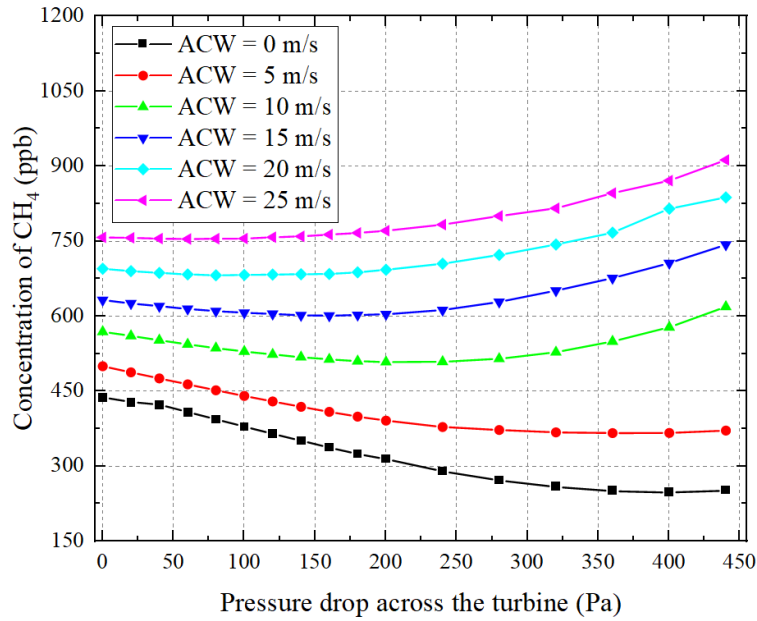
Fig.13. The concentration of CH_4 in the outlet of the SCPP-HPCR at $G = 857$ W/m^2.

3.4 SCPP-PPCR structure optimization

In the case of kilowatt-level SCPP, placing a blockage close to the collector entrance could diminish the adverse effects of ACW on the collector entrance but not on the chimney outlet [62]. The impact of the ACW on the output power of SCPP-PPCR and SCPP-HPCR, and SCPP with a blockage was shown in Fig. 14.
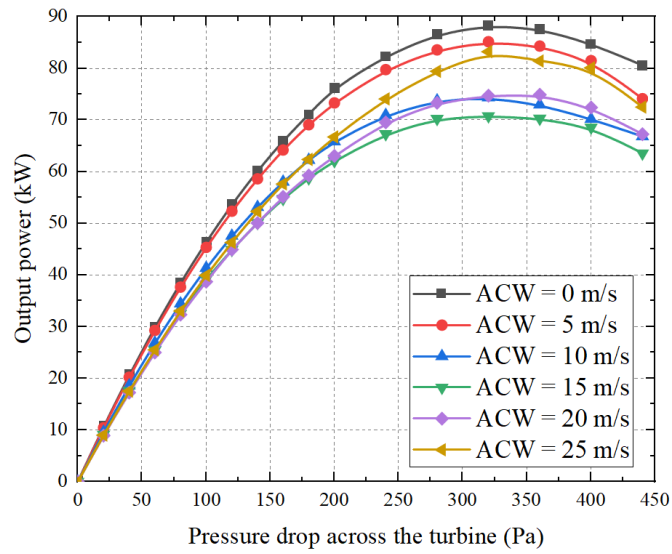
Regardless of the structures, the output power of the system was always at its maximum when the ACW = 0 m/s. The maximum output power of the SCPP-HPCR was more than that of the other two structures, and the corresponding turbine pressure drop also increased. For instance, when the ACW = 0 m/s, the maximum output power of the SCPP-PPCR was 54.23 kW, the SCPP with a blockage was 52.85 kW, and the SCPP-HPCR was 88.31 kW. Therefore, the SCPP-PPCR could optimize the structure of the SCPP to improve the power generation performance, which was 1.63 times that of SCPP and 1.67 times that of SCPP with a blockage. In addition, an excessive turbine pressure drop during the numerical computation procedure would make the solver unstable and eventually caused the calculation to diverge.
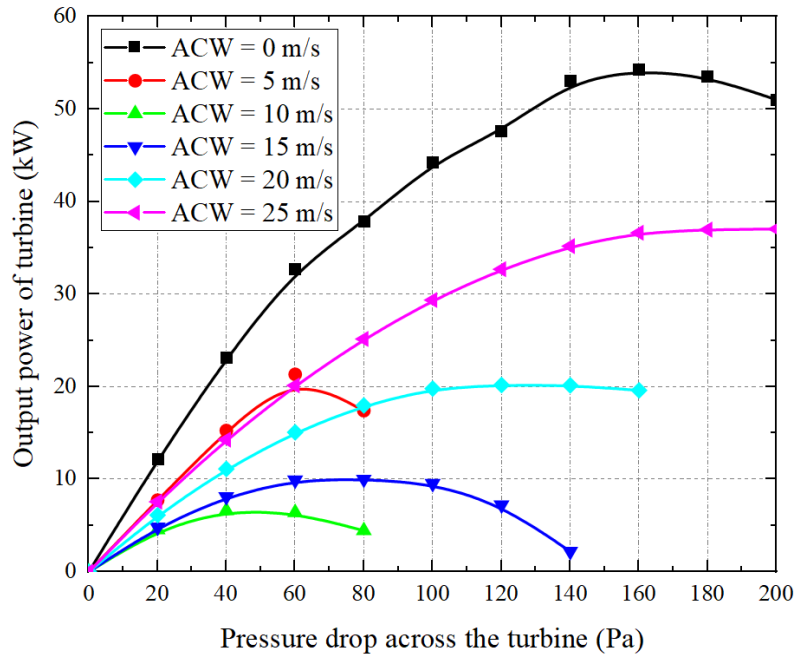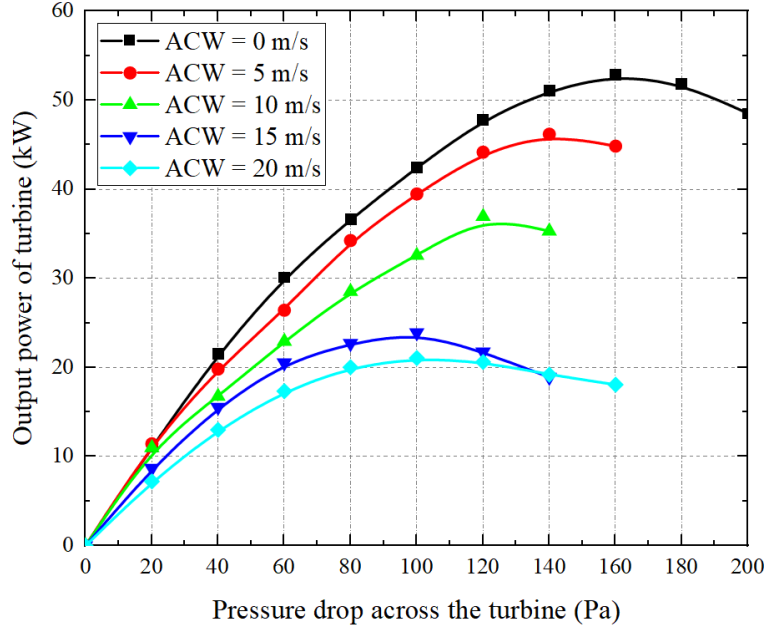
456
457

(a)

458
459

(b)

(c)

Fig.14. The output power of the SCPP with different structures at $G = 857$ W/m^2: (a)
SCPP-PPCR; (b) SCPP-HPCR; (c) SCPP with blockage [62].

3.5 Carbon dioxide emission reduction analysis

The carbon dioxide equivalent (C_{eq}) was a parameter to evaluate the total greenhouse effect. The non-CO_2 greenhouse gas emissions were converted into CO_2 emissions [74] by the following formula.

$$C_{eq} = \sum_{i=1}^{n} Q_i \times GWP_i \tag{18}$$

where Q_i was the emission of greenhouse gas i.

The CH$_4$ had a GWP value of 84 during the first 20 years after the emission, therefore one ton of CH$_4$ removal was equal to 84 tons of CO_2 emission reduction [53]. The main source of electricity in most countries was thermal power generation. But the burning of fossil fuels would emit a large amount of CO_2 into the atmosphere. It was reported that 0.95 kg of CO_2 was typically released every 1 kW-h of generation by a coal-fired power station [75]. The SCPP-PCRs could achieve CO_2 reduction and obtain clean power without harming the environment. In addition, the system degraded atmospheric CH$_4$ and produced equimolar CO_2. Consequently, the CO_2 reduction rate of the SCPP-PCRs was as follows:

$$\dot{C}_{eq} = \dot{m}_{CH_4} \times 84 + \dot{m}1_{CO_2} - \dot{m}2_{CO_2} \tag{19}$$

25

where $\dot{m}_{CH_4}$ represented the purification rate of CH4, $\dot{m}1_{CO_2}$ represented the reduction rate of CO_2 emission from coal-fired power station, $\dot{m}2_{CO_2}$ represented the generation rate of CO_2 from photocatalytic CH4.

Fig.15 showed the CO_2 emission reduction rate of the SCPP-HPCR at $G = 857$ W/m². The CO_2 emission reduction of the SCPP-HPCR could reach 85.04 kg/h when $G = 857$ W/m² and $\triangle P = 320$ Pa. The usage life of SCPP was between 80 and 120 years [76]. Considering the SCPP's building costs, the returns was produced after just 15 to 40 runs [77]. Furthermore, the P25 was a stable photocatalyst with long life [78]. If the SCPP-HPCRs were implemented, the economically efficient would be improved because of increased electricity generation, and CH4 was degraded on a large scale to achieve the goal of mitigating climate change.
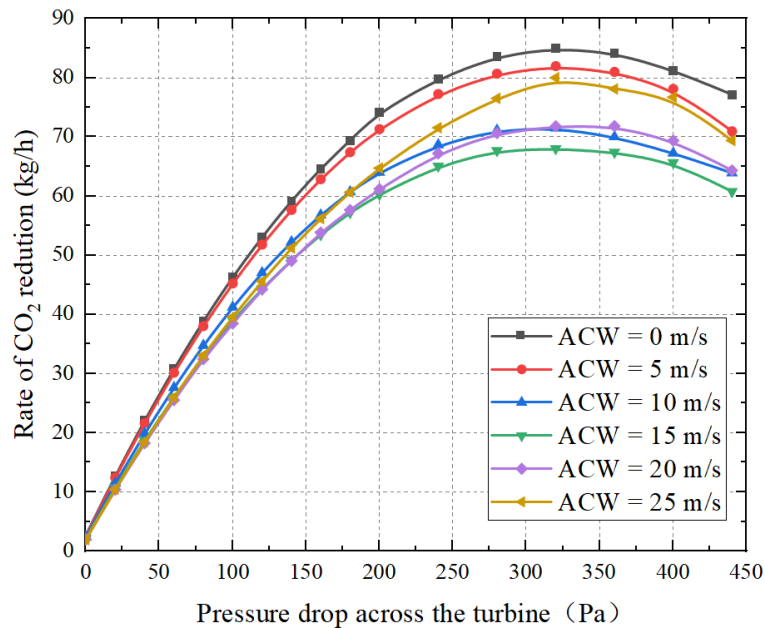
Fig.15. The rate of CO_2 reduction of the SCPP-HPCR at $G = 857$ W/m².

4. Conclusion

The SCPP-PCRs had enormous promise for combating climate change, but its ability to degrade CH4 in open spaces was unclear. A comprehensive numerical analysis was conducted for the SCPPs to study the potential using SCPP for atmospheric CH4 removal under the ACW. The conclusions were drawn as follows.

(1) In comparison to the SCPP-PPCR, the SCPP-HPCR could significantly improve the heat collection performance under ACW conditions.

(2) For the SCPP-PPCR, part of purified air escaped from the collector under the strong ACW conditions, but the SCPP-HPCR appeared to be more stable and controllable in CH_4 degradation.

(3) The mass flow rate significantly impacted on the rate of CH_4 decomposition. When ACW = 0 m/s, the SCPP-PPCR degraded CH_4 at a rate of 0.89 g/s compared to SCPP-HPCR's 0.54 g/s. The degradation rate of CH_4 of SCPP-PPCR reduced quickly and then stabilizes at 0.11 g/s when the ACW increases, whereas the rate of the SCPP-HPCR declined gradually and stabilizes at 0.41 g/s.

(4) The maximum power generation of SCPP-HPCR was 1.63 times that of SCPP and 1.67 times that of SCPP with a blockage. And the CO_2 emission reduction could reach 85.04 kg/h when $G = 857$ W/m^2, ACW = 0 m/s, and $\triangle P = 320$ Pa for a single SCPP-HPCR.

References

[1] M. Saunois, R. Jackson, P. Bousquet, B. Poulter, J. Canadell, The growing role of methane in anthropogenic climate change, Environmental Research Letters 11(12) (2016) 120207.

[2] J. Kuylenstierna, M. Zucca, M. Amann, B. Cardenas, B. Chambers, Z. Klimont, K. Hicks, R. Mills, L. Molina, F. Murray, Near-term climate protection and clean air benefits: Actions for Controlling Short-Lived Climate Forcers, (2011).

[3] K. Blok, W. Hare, N. Hohne, M. Kainuma, J. Kejun, D.S. Lee, J. Rogelj, A. Shukla, D. Arent, J. Bogner, Bridging the Emissions Gap: A UNEP Synthesis Report, United Nations Environment Programme (UNEP), 2011.

[4] N. Mengis, H.D. Matthews, Non-CO2 forcing changes will likely decrease the remaining carbon budget for 1.5 degrees C, Npj Climate and Atmospheric Science 3(1) (2020) 1-7.

[5] J.C. Kuylenstierna, E. Michalopoulou, C. Malley, Global Methane Assessment: Benefits and costs of mitigating methane emissions, (2021).

[6] R.P. Allan, E. Hawkins, N. Bellouin, B. Collins, IPCC, 2021: Summary for Policymakers, (2021).

[7] R.K. Pachauri, M.R. Allen, V.R. Barros, J. Broome, W. Cramer, R. Christ, J.A. Church, L. Clarke, Q. Dahe, P. Dasgupta, Climate change 2014: synthesis report. Contribution of Working Groups I, II and III to the fifth assessment report of the Intergovernmental Panel on Climate Change, Ipcc2014.

[8] T. Stocker, Climate change 2013: the physical science basis: Working Group I contribution to the Fifth assessment report of the Intergovernmental Panel on Climate Change, Cambridge university press2014.

[9] K. Kretschmer, A. Biastoch, L. Ruepke, E. Burwicz, Modeling the fate of methane hydrates under

global warming, Global Biogeochemical Cycles 29(5) (2015) 610-625.

[10] R. Jackson, E. Solomon, J. Canadell, M. Cargnello, C. Field, Methane removal and atmospheric restoration, Nature Sustainability 2(6) (2019) 436-438.

[11] H.D. Matthews, K. Caldeira, Stabilizing climate requires near-zero emissions, Geophysical Research Letters 35(4) (2008).

[12] A.E. Shilov, G.B. Shul'pin, Activation of C– H bonds by metal complexes, Chemical reviews 97(8) (1997) 2879-2932.

[13] R.P. Noceti, C.E. Taylor, J.R. D'Este, Photocatalytic conversion of methane, Catalysis today 33(1-3) (1997) 199-204.

[14] C.F. Lien, M.T. Chen, Y.F. Lin, J.L. Lin, Photooxidation of methane over TiO2, Journal of the Chinese Chemical Society 51(1) (2004) 37-42.

[15] T. Ming, W. Li, Q. Yuan, P. Davies, R. de Richter, C. Peng, Q. Deng, Y. Yuan, S. Caillol, N. Zhou, Perspectives on removal of atmospheric methane, Advances in Applied Energy 5 (2022) 100085.

[16] L. Yuliati, T. Hattori, H. Itoh, H. Yoshida, Photocatalytic nonoxidative coupling of methane on gallium oxide and silica-supported gallium oxide, Journal of Catalysis 257(2) (2008) 396-402.

[17] Y. Kato, H. Yoshida, T. Hattori, Photoinduced non-oxidative coupling of methane over silica-alumina and alumina around room temperature, Chemical Communications (21) (1998) 2389-2390.

[18] J. Wei, J. Yang, Z. Wen, J. Dai, Y. Li, B. Yao, Efficient photocatalytic oxidation of methane over β-Ga2O3/activated carbon composites, RSC Advances 7(60) (2017) 37508-37521.

[19] Z.H. Li, M.A. Boda, X.Y. Pan, Z.G. Yi, Photocatalytic Oxidation of Small Molecular Hydrocarbons over ZnO Nanostructures: The Difference between Methane and Ethylene and the Impact of Polar and Nonpolar Facets, Acs Sustainable Chemistry & Engineering 7(23) (2019) 19042-19049.

[20] Z. Li, X. Pan, Z. Yi, Photocatalytic oxidation of methane over CuO-decorated ZnO nanocatalysts, Journal of Materials Chemistry A 7(2) (2019) 469-475.

[21] X. Chen, Y. Li, X. Pan, D. Cortie, X. Huang, Z. Yi, Photocatalytic oxidation of methane over silver decorated zinc oxide nanocatalysts, Nature communications 7(1) (2016) 1-8.

[22] X. Pan, X. Chen, Z. Yi, Photocatalytic oxidation of methane over SrCO 3 decorated SrTiO 3 nanocatalysts via a synergistic effect, Physical Chemistry Chemical Physics 18(46) (2016) 31400-31409.

[23] R.J. Brenneis, E.P. Johnson, W. Shi, D.L. Plata, Atmospheric- and Low-Level Methane Abatement via an Earth-Abundant Catalyst, ACS Environmental Au   (2021).

[24] H. Dylla, M.M. Hassan, D. Osborn, Field Evaluation of Ability of Photocatalytic Concrete Pavements to Remove Nitrogen Oxides, Transportation Research Record: Journal of the Transportation Research Board 2290(1) (2012) 154-160.

[25] G.L. Guerrini, Photocatalytic performances in a city tunnel in Rome: NOx monitoring results, Construction and Building Materials 27(1) (2012) 165-175.

[26] M. Gallus, V. Akylas, F. Barmpas, A. Beeldens, E. Boonen, A. Boréave, M. Cazaunau, H. Chen, V. Daële, J. Doussin, Photocatalytic de-pollution in the Leopold II tunnel in Brussels: NOx abatement results, Building and Environment 84 (2015) 125-133.

[27] M. Gallus, R. Ciuraru, F. Mothes, V. Akylas, F. Barmpas, A. Beeldens, F. Bernard, E. Boonen, A. Boréave, M. Cazaunau, Photocatalytic abatement results from a model street canyon, Environmental Science and Pollution Research 22(22) (2015) 18185-18196.

[28] E. Boonen, V. Akylas, F. Barmpas, A. Boréave, L. Bottalico, M. Cazaunau, H. Chen, V. Daële, T. De Marco, J. Doussin, Construction of a photocatalytic de-polluting field site in the Leopold II tunnel in Brussels, Journal of Environmental Management 155 (2015) 136-144.

580 [29] H. Dylla, M.M. Hassan, D. Osborn, Field Evaluation of Ability of Photocatalytic Concrete
581 Pavements to Remove Nitrogen Oxides, Transport Res Rec 2290(2290) (2012) 154-160.

582 [30] W. Haaf, K. Friedrich, G. Mayr, J. Schlaich, Solar Chimneys Part I: Principle and Construction of
583 the Pilot Plant in Manzanares, International Journal of Solar Energy 2(1) (2007) 3-20.

584 [31] W. Haaf, Solar Chimneys, International Journal of Solar Energy 2(2) (2007) 141-161.

585 [32] N. Pasumarthi, S. Sherif, Experimental and theoretical performance of a demonstration solar
586 chimney model—Part I: mathematical model development, International Journal of Energy Research
587 22(3) (1998) 277-288.

588 [33] N. Pasumarthi, S. Sherif, Experimental and theoretical performance of a demonstration solar
589 chimney model—Part II: experimental and theoretical results and economic analysis, International
590 journal of energy research 22(5) (1998) 443-461.

591 [34] X.P. Zhou, F. Wang, J.A. Fan, R.M. Ochieng, Performance of solar chimney power plant in Qinghai-
592 Tibet Plateau, Renew Sust Energ Rev 14(8) (2010) 2249-2255.

593 [35] X.P. Zhou, S. Yuan, M.A.D. Bernardes, Sloped-collector solar updraft tower power plant
594 performance, International Journal of Heat and Mass Transfer 66 (2013) 798-807.

595 [36] Z. Akhtar, K.V.S. Rao, Theoretical Performance Analysis of Solar Chimney Power Plant for Kota
596 Region of Rajasthan, India, Applied Mechanics and Materials 787 (2015) 157-161.

597 [37] M.A.D. Bernardes, A. Voss, G. Weinrebe, Thermal and technical analyses of solar chimneys, Solar
598 Energy 75(6) (2003) 511-524.

599 [38] A. Koonsrisuk, Comparison of conventional solar chimney power plants and sloped solar chimney
600 power plants using second law analysis, Solar Energy 98 (2013) 78-84.

601 [39] A. Koonsrisuk, Mathematical modeling of sloped solar chimney power plants, Energy 47(1) (2012)
602 582-589.

603 [40] A. Koonsrisuk, T. Chitsomboon, Partial geometric similarity for solar chimney power plant
604 modeling, Solar Energy 83(9) (2009) 1611-1618.

605 [41] P.-h. Guo, J.-y. Li, Y. Wang, Numerical simulations of solar chimney power plant with radiation
606 model, Renewable energy 62 (2014) 24-30.

607 [42] X.P. Zhou, J.K. Yang, B. Xiao, G.X. Hou, Experimental study of temperature field in a solar chimney
608 power setup, Applied Thermal Engineering 27(11-12) (2007) 2044-2050.

609 [43] A.B. Kasaeian, E. Heidari, S.N. Vatan, Experimental investigation of climatic effects on the
610 efficiency of a solar chimney pilot power plant, Renew Sust Energ Rev 15(9) (2011) 5202-5206.

611 [44] M. Ghalamchi, A. Kasaeian, M. Ghalamchi, A.H. Mirzahosseini, An experimental study on the
612 thermal performance of a solar chimney with different dimensional parameters, Renewable Energy
613 91(Jun.) (2016) 477-483.

614 [45] N. Pasumarthi, S.A. Sherif, Experimental and theoretical performance of a demonstration solar
615 chimney model - Part II: Experimental and theoretical results and economic analysis, International
616 Journal of Energy Research 22(5) (1998) 443-461.

617 [46] C. Ketlogetswe, J.K. Fiszdon, O.O. Seabe, RETRACTED: Solar chimney power generation
618 project—The case for Botswana, Renewable and Sustainable Energy Reviews 12(7) (2008) 2005-2012.

619 [47] S. Kalash, W. Naimeh, S. Ajib, Experimental investigation of the solar collector temperature field
620 of a sloped solar updraft power plant prototype, Solar Energy 98 (2013) 70-77.

621 [48] A. Kasaeian, M. Ghalamchi, M. Ghalamchi, Simulation and optimization of geometric parameters
622 of a solar chimney in Tehran, Energy Conversion and Management 83 (2014) 28-34.

623 [49] O.K. Ahmed, A.S. Hussein, New design of solar chimney (case study), Case Studies in Thermal

Engineering 11 (2018) 105-112.

[50] A.G. Ferreira, C.B. Maia, M.F.B. Cortez, R.M. Valle, Technical feasibility assessment of a solar chimney for food drying, Solar Energy 82(3) (2008) 198-205.

[51] L. Zuo, Z.H. Liu, L. Ding, N. Qu, P.Z. Dai, B.F. Xu, Y. Yuan, Performance analysis of a wind supercharging solar chimney power plant combined with thermal plant for power and freshwater generation, Energy Conversion and Management 204 (2020).

[52] Q. Cao, D.Y. Pui, W. Lipinski, A concept of a novel solar-assisted large-scale cleaning system (SALSCS) for urban air remediation, Aerosol and air quality research 15(1) (2015) 1-10.

[53] R. de Richter, T.Z. Ming, P. Davies, W. Liu, S. Caillol, Removal of non-CO2 greenhouse gases by large-scale atmospheric solar photocatalysis, Prog Energ Combust 60 (2017) 68-96.

[54] O.M. Alfano, A.E. Cassano, Scaling-Up of Photoreactors: Applications to Advanced Oxidation Processes, Advances in Chemical Engineering 36 (2009) 229-287.

[55] M.M. Hossain, G.B. Raupp, S.O. Hay, T.N. Obee, Three-dimensional developing flow model for photocatalytic monolith reactors, AIChE Journal 45(6) (1999) 1309-1321.

[56] R. Yang, Y. Zhang, Q. Xu, J. Mo, A mass transfer based method for measuring the reaction coefficients of a photocatalyst, Atmospheric Environment 41(6) (2007) 1221-1229.

[57] T. Ming, H. Gui, T. Shi, H. Xiong, Y. Wu, Y. Shao, W. Li, X. Lu, R. de Richter, Solar chimney power plant integrated with a photocatalytic reactor to remove atmospheric methane: A numerical analysis, Solar Energy 226 (2021) 101-111.

[58] T. Ming, H. Xiong, T. Shi, Y. Wu, C. Wang, Y. Wen, W. Li, R. de Richter, N. Zhou, A novel green technology: Reducing carbon dioxide and eliminating methane from the atmosphere, International Journal of Energy Research   (2022) 1-14.

[59] M. Serag-Eldin, Mitigating adverse wind effects on flow in solar chimney plants, Proceedings of the 4th international engineering conference, Sharm El-Sheikh, 2004.

[60] X. Zhou, M.A.d.S. Bernardes, R.M. Ochieng, Influence of atmospheric cross flow on solar updraft tower inflow, Energy 42(1) (2012) 393-400.

[61] T.Z. Ming, X.J. Wang, R.K. de Richter, W. Liu, T.H. Wu, Y. Pan, Numerical analysis on the influence of ambient crosswind on the performance of solar updraft power plant system, Renew Sust Energ Rev 16(8) (2012) 5567-5583.

[62] T.Z. Ming, J.L. Gui, R.K. de Richter, Y. Pan, G.L. Xu, Numerical analysis on the solar updraft power plant system with a blockage, Solar Energy 98(-) (2013) 58-69.

[63] T.Z. Ming, Y.J. Wu, R.K. de Richter, W. Liu, S.A. Sherif, Solar updraft power plant system: A brief review and a case study on a new system with radial partition walls in its collector, Renew Sust Energ Rev 69 (2017) 472-487.

[64] J. Schlaich, The Solar Chimney Edition Axel Menges, Stuttgart, Germany   (1995).

[65] K. Rahbar, A. Riasi, Performance enhancement and optimization of solar chimney power plant integrated with transparent photovoltaic cells and desalination method, Sustainable Cities and Society 46 (2019) 101441.

[66] H. Pastohr, O. Kornadt, K. Gurlebeck, Numerical and analytical calculations of the temperature and flow field in the upwind power plant, International Journal of Energy Research 28(6) (2004) 495-510.

[67] T.Z. Ming, R.K. de Richter, F.L. Meng, Y. Pan, W. Liu, Chimney shape numerical study for solar chimney power generating systems, International Journal of Energy Research 37(4) (2013) 310-322.

[68] A. Haeger, O. Kleinschmidt, D. Hesse, Kinetics of photocatalyzed gas reactions using titanium dioxide as the catalyst part II: Photocatalyzed total oxidation of alkanes with oxygen, Chemical

Engineering & Technology: Industrial Chemistry-Plant Equipment-Process Engineering-Biotechnology 27(9) (2004) 1019-1026.

[69] X. Wang, X. Tan, T. Yu, Modeling of formaldehyde photocatalytic degradation in a honeycomb monolith reactor using computational fluid dynamics, Industrial & Engineering Chemistry Research 53(48) (2014) 18402-18410.

[70] J.E. Cermak, Applications of Fluid Mechanics to Wind Engineering—A Freeman Scholar Lecture, Journal of Fluids Engineering 97(1) (1975) 9-38.

[71] W. Haaf, Solar tower, part ii: Preliminary test results from the manzanares pilot plant, Solar Energy 2 (1984) 41-61.

[72] G.L. Xu, T.Z. Ming, Y.A. Pan, F.L. Meng, C. Zhou, Numerical analysis on the performance of solar chimney power plant system, Energy Conversion and Management 52(2) (2011) 876-883.

[73] R. Harte, R. Hoffer, W.B. Kratzig, P. Mark, H.J. Niemann, Solar updraft power plants: Engineering structures for sustainable energy generation, Engineering Structures 56 (2013) 1698-1706.

[74] Y. Pratiwi, A. Rejo, A. Fariani, M. Faizal, Source of Carbon Dioxide Emissions Equivalent to Plant-Based Control Concept with Dynamic System in Prabumulih City, South Sumatra Province, IOP Conference Series: Earth and Environmental Science 810(1) (2021) 012051.

[75] S.K. Guttikunda, P. Jawahar, Atmospheric emissions and pollution from the coal-fired thermal power plants in India, Atmospheric Environment 92 (2014) 449-460.

[76] R. Harte, R. Höffer, W.B. Krätzig, P. Mark, H.-J. Niemann, Solar updraft power plants: Engineering structures for sustainable energy generation, Engineering Structures 56(Complete) (2013) 1698-1706.

[77] W.B. Kratzig, Physics, computer simulation and optimization of thermo-fluidmechanical processes of solar updraft power plants, Solar Energy 98(-) (2013) 2-11.

[78] Q.P. Fan, X. Wang, Y.D. Li, Photo-catalytic activity and life time of the TiO2 nano-particles, Chinese Journal of Inorganic Chemistry 19(5) (2003) 521-526.